Nanoscale single-electron box with a floating lead for quantum sensing: Modeling and device characterization ⊘

N. Petropoulos ✉ 🅘 ; X. Wu 🅘 ; A. Sokolov 🅘 ; P. Giounanlis 🅘 ; I. Bashir 🅘 ; A. K. Mitchell 🅘 ; M. Asker;
D. Leipold 🅘 ; R. B. Staszewski 🅘 ; E. Blokhina ✉ 🅘

Check for updates

View Online   Export Citation

Nanoscale single-electron box with a floating lead for quantum sensing: Modeling and device characterization

View Online   Export Citation   CrossMark

N. Petropoulos,[1,2,3,a] (iD) X. Wu,[1,2,3] (iD) A. Sokolov,[3] (iD) P. Giounanlis,[3] (iD) I. Bashir,[4] (iD) A. K. Mitchell,[1,5] (iD) M. Asker,[4] (iD) D. Leipold,[4] (iD) R. B. Staszewski,[1,2,3] (iD) and E. Blokhina[1,2,3,a] (iD)

AFFILIATIONS

[1]Centre for Quantum Engineering, Science, and Technology (C-QuEST), Belfield, Ireland
[2]School of Electrical and Electronic Engineering, University College Dublin, Belfield, Ireland
[3]Equal1 Labs, Nexus UCD, Belfield, Ireland
[4]Equal1 Labs, Fremont, California 94536, USA
[5]School of Physics, University College Dublin, Belfield, Ireland

[a]Authors to whom correspondence should be addressed: nikolaos.petropoulos@ucdconnect.ie and elena.blokhina@ucd.ie

ABSTRACT

We present an in-depth analysis of a single-electron box (SEB) biased through a floating node technique that is common in charge-coupled devices. The device is analyzed and characterized in the context of single-electron charge sensing techniques for integrated silicon quantum dots (QD). The unique aspect of our SEB design is the incorporation of a metallic floating node, strategically employed for sensing and precise injection of electrons into an electrostatically formed QD. To analyze the SEB, we propose an extended multi-orbital Anderson impurity model (MOAIM), adapted to our nanoscale SEB system, that is used to predict theoretically the behavior of the SEB in the context of a charge sensing application. The validation of the model and the sensing technique has been carried out on a QD fabricated in a fully depleted silicon on insulator process (FD-SOI) on a 22-nm CMOS technology node. We demonstrate the MOAIM's efficacy in predicting the observed electronic behavior and elucidating the complex electron dynamics and correlations in the SEB. The results of our study reinforce the versatility and precision of the model in the realm of nanoelectronics and highlight the practical utility of the metallic floating node as a mechanism for charge injection and detection in integrated QDs. Finally, we identify the limitations of our model in capturing higher order effects observed in our measurements and propose future outlooks to reconcile some of these discrepancies.

Single-electron boxes (SEB) are a type of nanoscale electronic devices comprising a quantum dot (QD) coupled to a lead through a tunneling junction.[1] The chemical potential of the QD is controlled by a gate, coupled capacitively to it (implying no current flowing from the gate to the QD). The distinctive properties of single-electron boxes emerge as a consequence of their nanoscale dimensions, where the quantum nature of charge carriers becomes pronounced, giving rise to phenomena such as Coulomb blockade and quantum tunneling, especially at low temperatures.[2,3]

Quantum properties of SEBs make them extremely charge-sensitive, and these devices can be fabricated with precision engineering. In the light of the immense progress in semiconductor qubit technologies,[4] there is an increasing interest in sensitive electrometers

for silicon spin qubits that would take up a small area and be compatible with large scale integration. SEB electrometers have been proposed to be used as charge sensors for qubits[5–9] or even as quantum thermometers.[10] For that reason, probing the state of a SEB device made on a commercial process will be of benefit for developing quantum sensing applications.

In this paper, we present a SEB that is formed by a metallic node (lead) coupled to an electrostatically formed semiconductor QD. The key feature of this study is that the biasing and detecting of the SEB charge states is carried out through a scheme that is inspired by a technique common for the output stage of charge-coupled devices (CCDs).[11] It is worth noting that CCDs might also be addressing the problem of single-electron detection but in the context of

digital imaging.[12,13] Being essentially integrated systems, CCDs are particularly compatible with commercial and noncommercial semiconductor processes, and the measurement in CCDs is carried out in the charge domain. The feasibility of such biasing schemes has been demonstrated in Ref. 5. Moreover, quantum nanoelectronics devices lithographically defined in semiconducting 2D electron gas (2DEG) structures have been integrated recently with charge sensors to measure entropy changes in QD devices.[14,15]

The device is implemented in a commercial fully depleted silicon-on-insulator process on a 22-nm technological node by GlobalFoundries. Since the QD of the SEB is controlled electrostatically, we are interested in deriving its quantum mechanical model taking into account effective orbitals and potential shape formation fluctuations and asymmetries that are aspects of realistic QDs. For this reason, we develop a type of multi-orbital Anderson impurity model[16] (MOAIM) to predict the observed voltage from the SEB under the CCD biasing and measurement scheme. We then compare the SEB experimental characterization at a temperature of 3.5 K with the model and show that the SEB responds to individual charge transitions. This illustrates that it is possible to utilize SEB-CCD electrometers in integrated semiconductor QDs.

The system is presented in Fig. 1. The scheme of the SEB and its biasing principle are illustrated in Fig. 1(a). The SEB consists of an electrostatically defined semiconductor QD whose chemical potential

is controlled by the gate voltage V_g. There is a (metal) lead whose Fermi energy E_F is lying above the edge of its conduction band. The lead is connected to the QD through a tunneling junction. The Fermi energy of the lead is controlled by the biasing circuit in the following way. A switch is activated to connect the lead to a voltage source that elevates the potential of the lead to some $V_{pre-charge}$. The switch is deactivated after this, and the node is disconnected from the voltage source—it is in a "floating" state where any change in the number of electrons will result in a significant change of its electric potential due to its small capacitance. Next, the voltage V_g at the gate terminal is adjusted to tune the alignment of the Fermi energy of the lead to the chemical potential of the dot, allowing the tunneling of an electron from the lead to the QD. The second switch is then activated to measure if the electric potential of the lead has changed compared to the original state due to an electron tunneling to the QD. The capacitance of the lead is estimated (via parasitic extraction) to be 0.8 fF. The target design gain of the voltage amplifier is 80 (the gain is subject to process variability). This results in an expected $\sim$ 16 mV step at the output of the voltage amplifier per one electron removed from the lead to the QD. The temperature of the setup is 3.5 K.

The SEM image of the lead and the QD is shown in Fig. 1(b). While it is a part of a large QD array, we apply low voltages at all the gates. This results in a very large potential energy barrier separating the quantum dots from each other. We then can control the tunneling
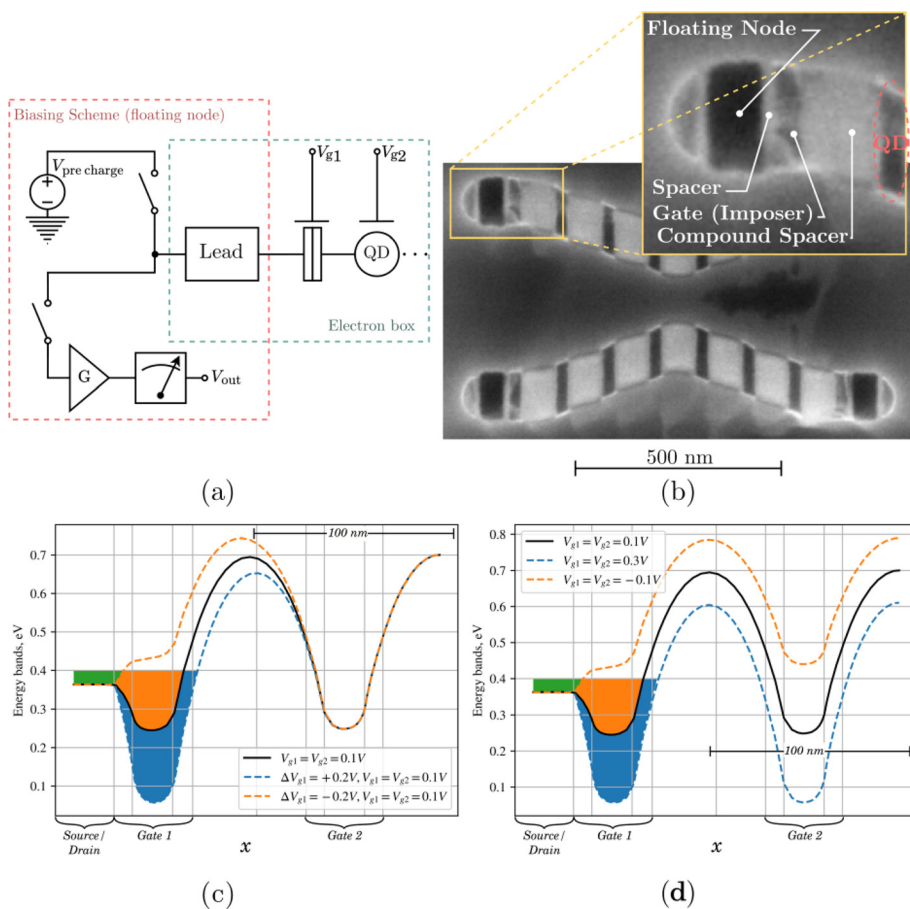

FIG. 1. (a) Schematic of the SEB device with its biasing scheme. (b) Scanning electron microscope (SEM) top-view image of sample B (more in the next figure). Inset picture shows the part of the device we are utilizing. The floating node is the electron reservoir (lead) coupled via a tunneling barrier to the QD. The tunneling barrier is effectively regulated by *gate* 1; *gate* 2 on the right is used to form the QD and to control its electrochemical potential. (c) and (d) QTCAD[17] self-consistent simulation of the conduction band, charge density, and Fermi level. On the horizontal axis, we plot the distance x (nm), and on the vertical axis, the energy $\mathcal{E}$ (eV). One well (colored) is formed under gate 1 adjacent to the lead; it is filled with electrons and forms an extended reservoir. The SEB well is formed under gate 2. Varying V_{g_1} lowers the tunneling barrier between the lead and the SEB QD. Figure (c) shows the tunneling barrier change with V_{g_1}. V_{g_2} manipulates the depth of the QD well. Figure (d) shows the QD depth change with V_{g_2}.

junction between the reservoir of electrons (lead) and the first quantum dot, while keeping the other dots isolated. The parameters of the devices are given in the figure caption.

The cross section view of the system is shown in Fig. 1(b). The thin Si-film results in a transversal confinement causing a 2DEG behavior of electrons in the film, and the in-plane confinement is controlled by the gates. In this class of devices, the formation of wells of the conduction band is defined electrostatically. The dot can form either below the gates or in the spaces between the gates depending on V_{g_i} and other controlled voltages (such as the common mode voltage V_{cm}). In the test presented in this paper, at $V_{\text{pre-charge}} = -410$ mV (after the pre-charge stage, the lead acquires a negative potential) and V_{g_i} ranging up to 0.3 V, a shallow well is formed below the gates (except for the very first one, adjacent to the lead that forms an extended electron reservoir due to diffusion on electrons). The self-consistent simulation of the conduction band and charge carrier density at 3.5 K, presented in the Figs. 1(c) and 1(d), confirms this assumption. (A single-gate test device was also tested by the means of transport measurement to confirm this.) In this study, we present the results of two different samples that have some variations in the shape of the lead, the spacer, and the gate.

In order to perform QD injection, spectroscopy, and characterization of its underlying physics, we first need to build a theoretical quantum model that can describe and predict the system's behavior. For the purpose of capturing the physical interactions and factors that contribute to the many-body dynamics of the QD, we employ an extended Fermi–Hubbard model for N effective quantum orbitals. The quantum model that describes the QD is expressed by the following Hamiltonian:

$$H_{QD} = \sum_{i=1}^{N} \sum_{\sigma \in \{\uparrow, \downarrow\}} \varepsilon_{i\sigma} n_{i\sigma} + \sum_{i \leq j} \sum_{\sigma, \sigma'} U_{ij,\sigma\sigma'} n_{i\sigma} n_{j\sigma'},$$

where $\varepsilon_{i\sigma}$ is the on-site potential for orbital i, $U_{ij,\sigma\sigma'}$ is the electrostatic Coulomb coupling between an electron at orbital i and spin σ and another electron at orbital j and spin σ' with $(i,\sigma) \neq (j,\sigma')$, $c_{i\sigma}^{(\dagger)}$ is the Fock space fermionic annihilation (creation) operator for a fermion at orbital i and spin σ, and $n_{i\sigma} = c_{i\sigma}^{\dagger} c_{i\sigma}$ is the number operator. The creation/annihilation operators satisfy the fermionic algebra anti-commutation relations $\{c_{j\sigma}, c_{k\sigma'}\} = \delta_{jk} \delta_{\sigma\sigma'}$ and $\{c_{j\sigma}^{\dagger}, c_{k\sigma'}^{\dagger}\} = \{c_{j\sigma}, c_{k\sigma'}\} = 0$ and act upon the system's Fock space; for $\mathcal{M}$ fermions, it is defined as $\mathfrak{F}_{\mathcal{M}} \equiv \oplus_{m=0}^{\mathcal{M}} \mathcal{H}_m$, with $\mathcal{H}_m = \mathcal{H}^{\otimes m}$ being the m—fermion Hilbert subspace.

For the physical specifications of our system, we have taken the QD to be of volume $v_{QD} = (80 \times 30 \times 6.25)$ nm^3 and to be composed of $N = 2$ effective orbitals for sample A and $N = 3$ for sample B; these are chosen phenomenologically and *ad hoc*. The dimensions of the dot are taken from the physical parameters of the system and will provide a very good correspondence to the observed energy levels. Since $d^{(z)} = 6.25$ nm $\ll d^{(x)}, d^{(y)}$ and so $\Delta \varepsilon^{(z)} \gg \Delta \varepsilon^{(x)}, \Delta \varepsilon^{(y)}$, we restrict ourselves to the orbitals formed due to confinement in the smaller $\hat{x}, \hat{y}$— dimensions. The contributing energies are the Coulomb intra- and inter-orbital coupling energies $U_{ij,\sigma\sigma'} = 3.1$ meV (Si), and the *effective* on-site confinement energies $\varepsilon_{i\sigma}^A \in \{1.56, 5.63\}$ (meV) and $\varepsilon_{i\sigma}^B \in \{1.56, 5.63, 10.91\}$ (meV), with $\varepsilon_{i\sigma} < \varepsilon_{j\sigma}$ for $i < j$. These are derived from a symmetric finite quantum well calculation, fine-tuned by a common mode voltage $V_{cm} \approx -427$ mV (which is close to the

−440 mV used in QTCAD), and since our formed QD need not be completely symmetrical, we add a random fluctuation of the energy levels to account for potential imperfections in our electrostatically formed QD. That is, we have $\varepsilon_{i\sigma}^X = \varepsilon_{k\sigma}^{X \,(ideal)} + \delta \varepsilon_{k\sigma}^{X \,(asym)}$, with $\delta \varepsilon_{k\sigma}^{X \,(asym)}$ sampled from a normal distribution $\mathcal{N}(\mu, \sigma^2)$ with mean $\mu = 0$ and standard deviation $\sigma = 20\%$. Finally, we utilize the transversal and longitudinal electron masses[18] as $m_t = 0.19 m_e$ (Si) and $m_l = 0.98 m_e$ (Si), respectively.

In addition to the above Hamiltonian that describes the dynamics of the isolated QD, we employ a lead Hamiltonian H_{lead}, which corresponds to the metallic floating node in the actual structure. We treat it as a semi-classical reservoir of electrons, from which they can jump in and out, with different energies $\{\lambda_{r\sigma}\}$ and a Fermi level E_F controlled externally through manipulation of a tunable electrochemical potential μ_{ch}. We include only a left lead ($\mathcal{L}$) coupled to the QD. In addition, we add the coupling between the lead and the QD (hybridization), so the total Hamiltonian for our SEB will have the form of a MOAIM,

$$H_{sys} = H_{lead} + H_{QD} + \sum_{r\sigma \in \mathcal{L}} \left(\tau_{r\sigma} w_{r\sigma}^{\dagger} c_{\sigma} + h.c. \right) \quad (1)$$

with $H_{\text{lead}} = \sum_{r\sigma \in \mathcal{L}} \lambda_{r\sigma} w_{r\sigma}^{\dagger} w_{r\sigma}$ with $\lambda_{r\sigma}$ the energy of the r level and spin σ of the metallic node Hamiltonian, $w_{r\sigma}^{(\dagger)}$ the fermionic annihilation (creation) operator of an electron of energy r level and spin σ in the lead, $\tau_{r\sigma}$ the hybridization (coupling) energy between each lead level and the QD, and $h.c.$ is the Hermitian conjugate counterterm.

We consider a uniform hybridization $\tau_{r\sigma} = \tau$, which is also manipulated via gate voltages ΔV_{g_i} in the device. In our simulation, its values range in the $\tau_{r\sigma} = 3 - 40$ μeV regime, which satisfies $\tau_{r\sigma} \ll \mathcal{E}$ for any energy scale $\mathcal{E}$ of our system. The full Hamiltonian H_{sys} can then be used to model the quantum transport properties of the system, and how the QD electronic occupation depends on applied potentials.[19–21]

We treat the QD in $\mathfrak{F}_{\mathcal{M}_{\max}}$ Fock space, allowing up to $\mathcal{M}_{\max} = 4$ and $\mathcal{M}_{\max} = 6$ electrons to occupy the structure for sample A and sample B, respectively. Our density matrix $\rho = \left\{ Q_{\mathcal{M}\mathcal{M}'}^{mm'} \right\}_{\mathcal{M}\mathcal{M}'}^{mm'}$, with $Q_{\mathcal{M}\mathcal{M}'}^{mm'} = |\mathcal{M}, m\rangle\langle\mathcal{M}', m'|$ the Hubbard operator has diagonal elements $P_{\mathcal{M}m}$, with $\sum_{\mathcal{M},m} P_{\mathcal{M}m} = 1$, and we show them symbolically in Table I. Each of the Fock eigenstates with $\mathcal{M}$ electrons will be a superposition of m states, with $m = \binom{\mathcal{M}_{\max}}{\mathcal{M}} = \frac{\mathcal{M}_{\max}!}{(\mathcal{M}_{\max} - \mathcal{M})! \, \mathcal{M}!}$.

We assume that the lead is weakly coupled to the QD and therefore keep up to second order hybridization terms $\mathcal{O}(\tau_{k\sigma}^2)$, so we can ignore off diagonal elements in ρ and significant mixing of Fock space states. Consequently, the dynamical evolution of the population numbers $P_{\mathcal{M}m} = P_{\mathcal{M}m}(t)$ is simplified to a set of partial differential master equations,[22]

$$\frac{\partial P_{00}}{\partial t} = -\frac{1}{\hbar} \sum_{m=1}^{\mathcal{M}_{\max}} \Gamma_{00,1m}^{res} \left[\bar{n}_{res}^{+}(\Delta_{1m,00}) P_{00} - \bar{n}_{res}^{-}(\Delta_{1m,00}) P_{1m} \right], \quad (2)$$

$$\begin{aligned} \frac{\partial P_{\mathcal{M}m}}{\partial t} = \frac{1}{\hbar} \sum_{m'} \Big\{ &\Gamma_{\mathcal{M}-1\,m',\mathcal{M}m}^{res} \left[\bar{n}_{res}^{+}(\Delta_{\mathcal{M}m,\mathcal{M}-1\,n'}) P_{\mathcal{M}-1\,m'} \right. \\ &- \bar{n}_{res}^{-}(\Delta_{\mathcal{M}m,\mathcal{M}-1\,m'}) P_{\mathcal{M}m} \big] - \Gamma_{\mathcal{M}m,\mathcal{M}+1\,n'}^{res} \\ &\times \left[\bar{n}_{res}^{+}(\Delta_{\mathcal{M}+1\,m',\mathcal{M}m}) \times P_{\mathcal{M}m} \right. \\ &- \bar{n}_{res}^{-}(\Delta_{\mathcal{M}+1\,n',\mathcal{M}m}) P_{\mathcal{M}+1\,m'} \big] \Big\}, \quad (3) \end{aligned}$$

TABLE I. Table of the allowed Fock eigenstates $|\mathcal{M}, m\rangle$ of the QD Hamiltonian H_{QD} of each Fock subspace. The states' coefficients α_{mk}, β_{mk}, ..., depend on the parameters of the system $\varepsilon_{i\sigma}$, $U_{jk,\sigma\sigma'}$ which are in turn dependent on the physical architecture of the QDs and control voltages v_{QD}, V_g, ΔV_{g_1}; we include here the compact expressions, since the full ones are very complex and long to write out explicitly. The states are denoted as $|s_1; s_2; \ldots; s_N\rangle \equiv \otimes_{n=1}^{N}|s_n\rangle$, with s_k the $\hat{z}-$ spin projection of the kth$-$QD level occupation. We label with m_i^* the maximum value of m_i for $\mathfrak{F}_i$ and with m^* its overall maximum value.

Number of electrons ν_{e^-}	Fock space eigenstate $|\mathcal{M}, m\rangle$
0	$|0, 1\rangle = |0; 0; \ldots; 0\rangle$
1	$|1, m_1\rangle = \sum_{k=1}^{m_1} \alpha_{m_1 k}|s_{1_{m_1 k}}; s_{2_{m_1 k}}; \ldots; s_{N_{m_1 k}}\rangle,$ $m_1 \in \left\{1, \ldots, \binom{\mathcal{M}_{\max}}{1}\right\}$
2	$|2, m_2\rangle = \sum_{k=1}^{m_2} \beta_{m_2 k}|s_{1_{m_2 k}}; s_{2_{m_2 k}}; \ldots; s_{N_{m_2 k}}\rangle,$ $m_2 \in \left\{m_1^* + 1, \ldots, m_1^* + \binom{\mathcal{M}_{\max}}{2}\right\}$
⋮	⋮
$\mathcal{M}_{\max}$	$|\mathcal{M}_{\max}, m^*\rangle = |\uparrow\downarrow; \uparrow\downarrow; \ldots; \uparrow\downarrow\rangle$

$$\frac{\partial P_{\mathcal{M}_{\max} m^*}}{\partial t} = \frac{1}{\hbar} \sum_{m=1}^{\mathcal{M}_{\max}} \Gamma_{\mathcal{M}_{\max}-1\, m, \mathcal{M}_{\max} m^*}^{res} \left[\bar{n}_{res}^{+}\left(\Delta_{\mathcal{M}_{\max} m^*, \mathcal{M}_{\max}-1\, m}\right)\right.$$
$$\left. \times P_{\mathcal{M}_{\max}-1\, m} - \bar{n}_{res}^{-}(\Delta_{\mathcal{M}_{\max} m^*, \mathcal{M}_{\max}-1\, m}) P_{\mathcal{M}_{\max} m^*}\right],$$
(4)

where $\Gamma_{\mathcal{M}m, \mathcal{M}'m'}^{res} = 2\pi \sum_{r\sigma \in \mathscr{L}} |\tau_{r\sigma} \alpha_{\mathcal{M},\mathcal{M}'}^{mm'}|^2 \delta(\Delta_{\mathcal{M}'m', \mathcal{M}m} - \lambda_{r\sigma})$ is the tunneling rate between the metallic lead and the QD with $\Delta_{\mathcal{M}m, \mathcal{M}'m'} \equiv E_{\mathcal{M}m} - E_{\mathcal{M}'m'}$ the energy difference between the two

Fock eigenstates, $\alpha_{\mathcal{M},\mathcal{M}'}^{mm'} \equiv \langle \mathcal{M}, m|c_\sigma|\mathcal{M}', m'\rangle$ the transition elements, $\delta(x - \varepsilon_{r\sigma})$ the Dirac delta function, $\bar{n}_{res}^{+}(x) = \frac{1}{e^{(x-\mu_{ch})/k_B T}+1}$ the Fermi–Dirac statistical function, and $\bar{n}_{res}^{-}(x) = 1 - \bar{n}_{res}^{+}(x)$.

Initializing our system with no electrons in it, $P_{00}(t = 0) = 1$, we show the dependence of the population numbers close to equilibrium (steady state), with respect to μ_{ch} of the lead in Fig. 2(a) for sample A and Fig. 2(c) for sample B, respectively. We can see the dynamical evolution of the Fock states to approach thermal equilibrium in Fig. 2(b) for sample A and in Fig. 2(d) for sample B. Given some initial conditions, there is a clear threshold lead electrochemical potential (i.e., gate voltage V_g) $\mu_{ch,th}$ for which we have a many-body stochastic injection in the structure, which is related to the energy level spacing between the lead and the first non-trivial Fock state of the QD. Using the population numbers and the corresponding electron number $\nu(\mu_{ch})$ of each Fock state, we can compute an average,

$$\langle \nu_T(\mu_{ch})\rangle \equiv \mathbb{E}[\nu_T(\mu_{ch})] = \sum_{\mathcal{M}=0}^{\mathcal{M}_{\max}} \sum_{m}^{m_{\max}} \nu_{\mathcal{M}m}(\mu_{ch}, T) \times P_{\mathcal{M}m}(\mu_{ch}, T),$$
(5)

where $\nu_{\mathcal{M}m}(\mu_{ch}, T)$ and $P_{\mathcal{M}m}(\mu_{ch}, T)$ is the number of electrons and occupation number of state $|\mathcal{M}, m\rangle$ in the QD for an electrochemical potential μ_{ch} and temperature T, respectively.

We can connect $\nu(\mu_{ch})$ to the actual voltage measurements in our detectors using the transformation functions $\langle V_{out}^A\rangle \approx -23 \langle \nu_T\rangle$ mV and $\langle V_{out}^B\rangle \approx -16 \langle \nu_T\rangle$ mV, where V_{out}^X is the experimentally measured voltage on structure X, as we show in Fig. 3. Here, we plot the obtained $\langle V_{out}^X\rangle$ as a function of the applied gate voltage V_g in order to describe approximately the measured voltage drop. We use the transformation function $V_g = 8\,\mu_{ch}\,(V/eV)$ obtained from QTCAD simulations. Moreover, to account for the effects of noise in the measurement, we use a Gaussian noise filter in our calculated output observable. That is, we plot $\langle \tilde{V}_{out}^X\rangle = \langle V_{out}^X\rangle \times \mathscr{G}_{noise}$, where
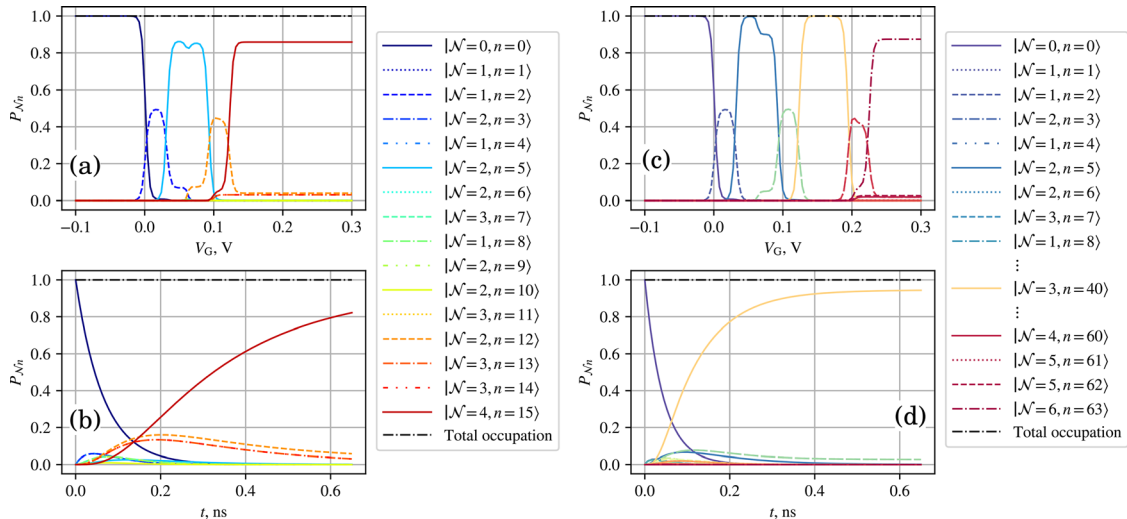
FIG. 2. Fock state occupancy probabilities $P_{\mathcal{N}n}$ at $T = 3.5\,K$ and hybridization energy $\tau_{k\sigma} = 20\,\mu$ eV. Probability plots as functions of different system parameters. (a) Fock states' occupancies $P_{\mathcal{N}n}$ as a function of applied voltage V_g sweep for sample A for $t \approx 0.6$ ns. (b) Dynamical evolution of Fock states occupancies as a function of time, for $V_g \approx 0.18$ V for sample A. (c) The same as (a) but for the model corresponding to sample B. We see more plots, because we consider $N = 3$ orbitals in the model for this sample, so we can have up to a maximum of $\mathcal{N}_{\max} = 6$ electrons present in the QD and a total of 64 states. (d) The same as (b) but for the model corresponding to sample B.
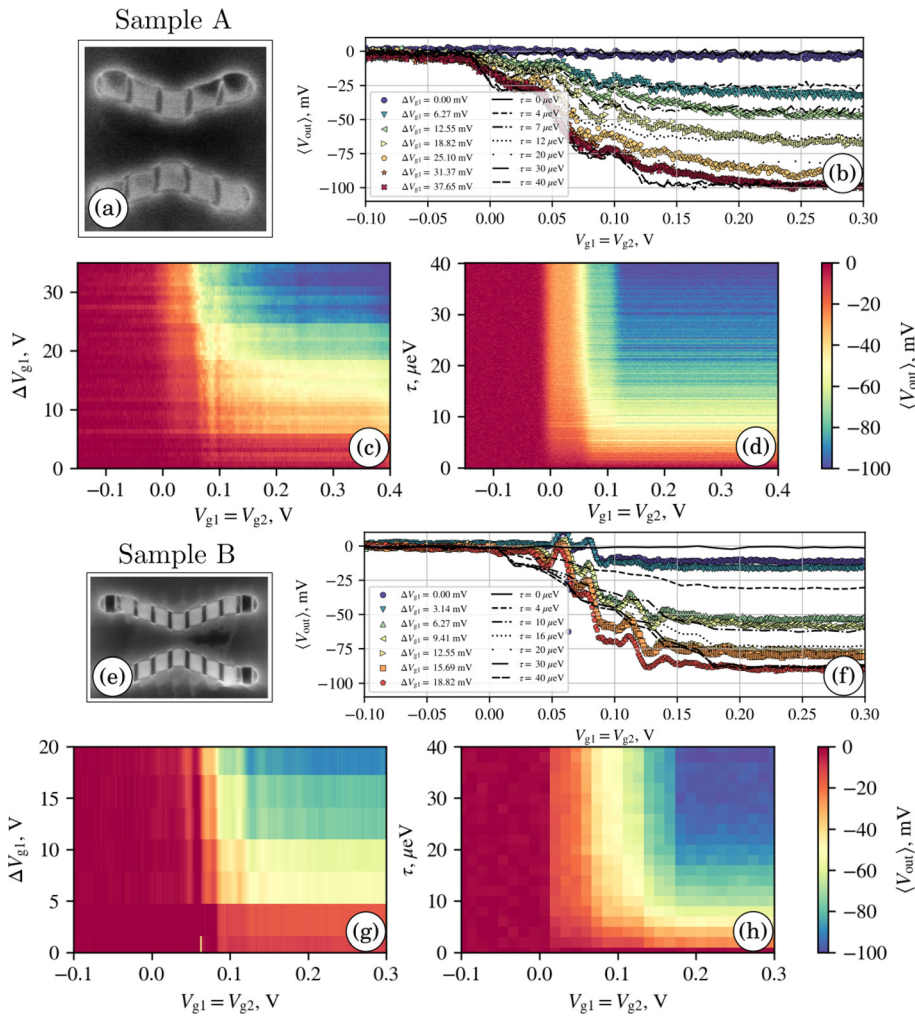
FIG. 3. Injections line-plots and heatmaps for two different structures, labeled sample A and sample B. (a) Sample A architecture. (b) Lineplots of experimental measurements (colored dots) and theoretical predictions (black dashed lines) for sample A. (c) Heatmap produced from the experiment of sample A structure. (d) Heatmap produced from our MOAIM for the same structure; in the transversal axis, we have left the hybridization energy units from the model. (e) Sample B architecture. (f) Lineplots of experimental measurements (colored dots) and theoretical predictions (black dashed lines). Again, we have left the model hybridization energies in their original expressions. (g) Heatmap produced from experimental measurements for sample B. (h) Heatmap produced from our MOAIM for the same structure.

$\mathcal{G}_{noise} \in \mathcal{N}(\mu, \sigma^2)$ with $\mu = 1$ and $\sigma = 4\%$, for both structures. Sweeping over V_g and ΔV_{g_1} voltages in the experiment corresponds to sweeping over μ_{ch} and τ in our model.

As a conclusion, we would like to highlight some key points of this work. First, we showed that the resolution of our device is sensitive to single-electron injection within some variance induced by thermal noise due to finite operating temperature. This shows that both the device and the incorporation of a metallic floating node with standard CCD circuitry are efficient in relevant quantum charge sensing applications. Moreover, the agreement between our simulations from QTCAD and MOAIM with the experimentally measured data further hints at the device behaving as an SEB and a QD forming under gate 2. The predictions of the MOAIM are compatible both with the applied voltages and the QD geometry in the actual device, and it captures effectively the most significant aspects of the experiment. These are the measured voltage at electron injection plateaus (quantized charge and Coulomb blockade), the stretching of the curves when the coupling between metallic node and the QD is varied $(\partial \langle V_{out}^X \rangle / \partial \tau > 0)$ and the average decrease in the variation between curve gaps $(\partial^2 \langle V_{out}^X \rangle / \partial \tau^2 < 0)$.

On the other hand, there are some potentially interesting physics that our model does not capture. Some of these are the small "S" shaped bumps in the experimental data, which are located where injection happens (more apparent in sample B) and the voltage-dependent drift in the experimental curves (more apparent in sample A). Finally, one can in principle go beyond the semi-classical rate-equation treatment presented above to include QD-lead entanglement effects,[23] renormalization phenomena at low-temperatures, and spin-flip scattering producing more subtle quantum behavior such as the Kondo effect.[24] We leave all of the aforementioned as interesting outlooks for future research.

AUTHOR DECLARATIONS
Conflict of Interest

The authors have no conflicts to disclose.

Author Contributions

N. Petropoulos: Data curation (supporting); Formal analysis (lead); Investigation (equal); Methodology (equal); Validation (equal);

DATA AVAILABILITY

The data that support the findings of this study are available from the corresponding authors upon reasonable request.

REFERENCES

[1]Y. V. Nazarov and Y. M. Blanter, *Quantum Transport: Introduction to Nanoscience* (Cambridge University Press, 2009).

[2]P. Yadav, S. Chakraborty, D. Moraru, and A. Samanta, "Variable-barrier quantum coulomb blockade effect in nanoscale transistors," Nanomaterials **12**, 4437 (2022).

[3]S. Goodnick and J. Bird, "Quantum-effect and single-electron devices," IEEE Trans. Nanotechnol. **2**, 368–385 (2003).

[4]J. Anders, J. C. Bardin, I. Bashir, G. Billiot, E. Blokhina, S. Bonen, E. Charbon, J. Chiaverini, I. L. Chuang, C. Degenhardt *et al.*, "CMOS integrated circuits for the quantum information sciences," IEEE Trans. Quantum Eng. **4**, 5100230 (2023).

[5]I. Bashir, E. Blokhina, A. Esmailiyan, D. Leipold, M. Asker, E. Koskin, P. Giounanlis, H. Wang, D. Andrade-Miceli, A. Sokolov *et al.*, "A single-electron injection device for CMOS charge qubits implemented in 22-nm FD-SOI," IEEE Solid-State Circuits Lett. **3**, 206–209 (2020).

[6]M. J. Filmer, T. A. Zirkle, J. Chisum, A. O. Orlov, and G. L. Snider, "Using single-electron box arrays for voltage sensing applications," Appl. Phys. Lett. **116**, 213103 (2020).

[7]C. Power, D. Andrade-Miceli, I. Bashir, M. Asker, D. Leipold, R. B. Staszewski, and E. Blokhina, "Modelling of electron injection and confinement in cryogenic 22-nm FD-SOI quantum dot arrays," in *29th IEEE International Conference on Electronics, Circuits and Systems (ICECS)* (IEEE, 2022), pp. 1–4.

[8]G. A. Oakes, V. N. Ciriano-Tejel, D. F. Wise, M. A. Fogarty, T. Lundberg, C. Lainé, S. Schaal, F. Martins, D. J. Ibberson, L. Hutin, B. Bertrand, N. Stelmashenko, J. W. A. Robinson, L. Ibberson, A. Hashim, I. Siddiqi, A. Lee, M. Vinet, C. G. Smith, J. J. L. Morton, and M. F. Gonzalez-Zalba, "Fast high-fidelity single-shot readout of spins in silicon using a single-electron box," Phys. Rev. X **13**, 011023 (2023).

[9]G. Mihailescu, A. Bayat, S. Campbell, and A. K. Mitchell, "Multiparameter critical quantum metrology with impurity probes," arXiv:2311.16931 [quant-ph] (2023).

[10]G. Mihailescu, S. Campbell, and A. K. Mitchell, "Thermometry of strongly correlated fermionic quantum systems using impurity probes," Phys. Rev. A **107**, 042614 (2023).

[11]J. R. Janesick, T. S. Elliott, A. Dingiziam, R. A. Bredthauer, C. E. Chandler, J. A. Westphal, and J. E. Gunn, "New advancements in charge-coupled device technology: Subelectron noise and 4096 x 4096 pixel CCDs," Proc. SPIE **1242**, 223–237 (1990).

[12]O. Abramoff, L. Barak, I. M. Bloch, L. Chaplinsky, M. Crisler, A. Drlica-Wagner, R. Essig, J. Estrada, E. Etzion, G. Fernandez *et al.*, "Sensei: Direct-detection constraints on sub-GeV dark matter from a shallow underground run using a prototype skipper CCD," Phys. Rev. Lett. **122**, 161801 (2019).

[13]J. Tiffenberg, M. Sofo-Haro, A. Drlica-Wagner, R. Essig, Y. Guardincerri, S. Holland, T. Volansky, and T.-T. Yu, "Single-electron and single-photon sensitivity with a silicon skipper CCD," Phys. Rev. Lett. **119**, 131802 (2017).

[14]T. Child, O. Sheekey, S. Lüscher, S. Fallahi, G. C. Gardner, M. Manfra, A. Mitchell, E. Sela, Y. Kleeorin, Y. Meir, and J. Folk, "Entropy measurement of a strongly coupled quantum dot," Phys. Rev. Lett. **129**, 227702 (2022).

[15]C. Han, Z. Iftikhar, Y. Kleeorin, A. Anthore, F. Pierre, Y. Meir, A. K. Mitchell, and E. Sela, "Fractional entropy of multichannel kondo systems from conductance-charge relations," Phys. Rev. Lett. **128**, 146803 (2022).

[16]A. C. Hewson, *The Kondo Problem to Heavy Fermions*, Cambridge Studies in Magnetism (Cambridge University Press, 1993).

[17]Nanoacademic Technologies Inc., see https://docs.nanoacademic.com/qtcad/theory/poisson/ for "QTCAD finite-element-based simulation platform for quantum technology."

[18]C. Kittel, *Introduction to Solid State Physics*, 8th ed. (John Wiley & Sons, Nashville, TN, 2004).

[19]L. P. Kouwenhoven, C. M. Marcus, P. L. McEuen, S. Tarucha, R. M. Westervelt, and N. S. Wingreen, "Electron transport in quantum dots," in *Mesoscopic Electron Transport* (Springer, 1997), pp. 105–214.

[20]W. Shangguan, T. A. Yeung, Y. Yu, and C. Kam, "Quantum transport in a one-dimensional quantum dot array," Phys. Rev. B **63**, 235323 (2001).

[21]S. Gurvitz, "Rate equations for quantum transport in multidot systems," Phys. Rev. B **57**, 6602 (1998).

[22]J. Fransson and M. Råsander, "Pauli spin blockade in weakly coupled double quantum dots," Phys. Rev. B **73**, 205333 (2006).

[23]E. L. Minarelli, J. B. Rigo, and A. K. Mitchell, "Linear response quantum transport through interacting multi-orbital nanostructures," arXiv:2209.01208 [cond-mat.str-el] (2022).

[24]A. K. Mitchell, D. E. Logan, and H. Krishnamurthy, "Two-channel kondo physics in odd impurity chains," Phys. Rev. B **84**, 035119 (2011).